

1       **A Modified Dual-Wavelength Technique for Ku- and Ka-band Radar Rain Retrieval**

2  
3                   Liang Liao<sup>1</sup> and Robert Meneghini<sup>2</sup>

4  
5                   <sup>1</sup> Goddard Earth Science Technology & Research, Morgan State University, MD

6                   <sup>2</sup> NASA Goddard Space Flight Center, Greenbelt, MD

7  
8  
9  
10  
11  
12                   Submitted to  
13                   Journal of Applied Meteorology and Climatology  
14  
15  
16  
17  
18  
19  
20  
21  
22  
23  
24  
25  
26  
27  
28  
29  
30

31   Corresponding author information:

32  
33   Dr. Liang Liao  
34   Goddard Earth Science Technology/MSU  
35   Code 612  
36   NASA/Goddard Space Flight Center  
37   Greenbelt, MD 20771  
38  
39   301-614-5718 (phone)  
40   301-614-5492 (fax)  
41   Email: Liang.Liao-1@ nasa.gov  
42  
43

## Abstract

To overcome a deficiency in the standard Ku- and Ka-band dual-wavelength radar technique, a modified version of the method is introduced. The deficiency arises from ambiguities in the estimate of the mass-weighted diameter ( $D_m$ ) of the raindrop size distribution (DSD) derived from the differential frequency ratio (DFR), defined as the difference between the radar reflectivity factors in dB at Ku- and Ka-band,  $Z_{Ku}-Z_{Ka}$ . In particular, for DFR values less than zero, there are two possible solutions of  $D_m$ , leading to ambiguities in the retrieved DSD parameters. It is shown that the double solutions to  $D_m$  are effectively eliminated if the DFR is modified from  $Z_{Ku}-Z_{Ka}$  to  $Z_{Ku}-\gamma Z_{Ka}$  (in dB) where  $\gamma$  is a constant with a value less than 0.8. An optimal radar algorithm that uses the modified DFR for the retrieval of rain and  $D_m$  profiles is described. The validity and accuracy of the algorithm are tested by applying it to radar profiles that are generated from measured DSD data. Comparisons of the rain rates and  $D_m$  estimated from the modified DFR algorithm to the same hydrometeor quantities computed directly from the DSD spectra (or the truth) indicate that the modified DFR-based profiling retrievals perform fairly well, and are superior in accuracy and robustness to retrievals using the standard DFR.

## 1. Introduction

There is an increasing trend of using multiple wavelength radars in an effort to accurately detect and retrieve cloud and precipitation microphysical properties. The dual-wavelength radar is, however, the most popular among these applications. It makes use of two wavelengths, one of which is such that Rayleigh scattering dominates for most precipitation-sized particles and the other short enough so that non-Rayleigh (or Mie) scattering occurs in the presence of large hydrometeors. For precipitation measurements, the combination of Ku- (or X-) and Ka-band is found in many air/space-borne radar applications. This choice is dictated not only by the desire for microphysical information but by practical considerations such as frequency allocation (for space-based radars), the advantages of matched radar beams, and the desire for good spatial resolution within the constraints of antenna size. Attenuation caused by rain and mixed-phase hydrometeors, among other factors, is also important in choosing frequencies not only because it adds difficulty in estimating precipitation but because it often prevents the radar signal from penetrating the entire storm.

The Dual-wavelength Precipitation Radar (DPR) operating at Ku- and Ka-band, aboard the Global Precipitation Measurement (GPM) core satellite, is the first dual-wavelength radar in space (Hou et al. 2008). An important goal of the DPR is to derive rain rate and raindrop size distribution (DSD), the latter of which is often modeled by an analytical function (Ulbrich, 1983; Gorgucci et al. 2000 and 2002; Bringi et al. 2002; Feingold and Levin 1986). Several dual-wavelength radar retrieval techniques have been developed which are based on the standard dual-wavelength technique that uses the differential frequency ratio (DFR), i.e., the difference of radar reflectivities between two wavelengths, to first infer the DSD parameters, correct attenuation and then derive the rain rate profile gate by gate either stepping forward or backward

1 along the radar beam (Meneghini et al. 1992 and 1997; Mardiana et al. 2004; Liao and  
2 Meneghini 2005; Rose and Chandrasekar 2005; Seto et al. 2013; Seto and Iguchi 2015; Liao et  
3 al. 2016). To improve the robustness of the dual-wavelength retrieval, several optimal estimation  
4 methods have been recently proposed, including the GPM DPR (version-5) algorithm, in which  
5 one or more adjustment factors are used to modify nominal relationships between the parameters  
6 of the radar and the precipitation (such as  $k$ - $Z$  and  $R$ - $D_m$  relations, where  $k$ ,  $Z$ ,  $R$  and  $D_m$  are  
7 specific attenuation, radar reflectivity, rain rate and mass-weighted diameter) to account for  
8 variations in the DSD in space and time (Grecu et al. 2011; Seto and Iguchi 2015). Adjustment  
9 factors at each gate/profile are determined by optimizing predefined cost functions that constrain  
10 the values of the reflectivities and path integral attenuations (PIA).

11 In the standard DFR-based dual-wavelength technique the two unknown DSD parameters,  
12 related to the characteristic size and number density of raindrops, are estimated at each range  
13 gate. However, this is successful only if there exist unique solutions of the DSD parameters to  
14 the dual-wavelength radar equations. For the gamma DSD model, ambiguities in the estimation  
15 of  $D_m$  often occur, particularly for light-to-moderate rain rates. As there is no additional  
16 information aiding in selection of the solution, the standard dual-wavelength technique becomes  
17 problematic for rain retrievals. Retrieval errors caused by improper selection of the solution  
18 worsen as retrieval proceeds deep into the storm as a result of error propagation. It has been  
19 revealed in our study from a large collection of the measured DSD data from various NASA-  
20 sponsored field campaigns that negative DFR values occur frequently. Since these negative DFR  
21 values lead to ambiguities in the estimate of  $D_m$  and therefore  $N_w$  and further that these errors are  
22 propagated in range because of attenuation correction, the overall performance of the dual-  
23 frequency retrieval will be adversely affected.

To circumvent the double-value problem of  $D_m$ , a modified DFR, denoted by  $DFR^*$ , is introduced in this study. Instead of weighting equally the Ku- and Ka-band reflectivities, the  $DFR^*$  weights the Ka-band reflectivity less than the Ku-band so that the possibility of double solutions diminishes. Removal of the double values of  $D_m$  with use of  $DFR^*$  aids in finding  $D_m$  unambiguously from the  $D_m$ - $DFR^*$  relations; the trade-off, however, is that the  $DFR^*$  is no longer exclusively a function of  $D_m$  but a function of the number concentration parameter as well.

In this study, our focus is on examining the potential of  $DFR^*$  for the retrieval of the vertical rain and DSD profiles by employing measured DSD data. For understanding the uncertainties in rain rate estimation and also in gaining insight into ways to improve the algorithms, a physical evaluation of the standard (DFR-based) and modified ( $DFR^*$ -based) dual-wavelength techniques is conducted by applying them to simulated vertical rain profiles. The hydrometeor profiles for use in our evaluation are constructed by using the measured DSD acquired from various storm systems.

In this paper we begin with briefly describing the principle and issues associated with the standard dual-wavelength technique in Section 2, followed by the discussion of the modified dual-wavelength technique in Section 3. Described in Section 4 are the methodology related to the radar profiling algorithms and their procedures for the retrieval of rain and DSD profiles using the DFR and  $DFR^*$  while evaluation of the performance of the profiling algorithms is made in Section 5. Summary and remarks are given in Section 6.

## **2. Standard Dual-Wavelength Radar Technique**

The measured radar reflectivity factor ( $z_m$  in  $\text{mm}^6/\text{m}^3$ ) of the hydrometeors at range  $r$  and at wavelength  $\lambda$  can be expressed as

$$z_m = z_e \exp(-0.2 \ln(10) \int_0^r k dr), \quad (1)$$

where  $z_e$  is the effective radar reflectivity factor ( $\text{mm}^6/\text{m}^3$ ) and  $k$  is specific attenuation ( $\text{dB}/\text{km}$ ), expressed as

$$z_e = \frac{\lambda^4}{\pi^5 |K_w|^2} \int_0^\infty N(D) \sigma_b(D, \lambda) dD \quad (2)$$

and

$$k = 4.343 \times 10^{-3} \int_0^\infty N(D) \sigma_e(D, \lambda) dD, \quad (3)$$

where  $\sigma_b(D, \lambda)$  and  $\sigma_e(D, \lambda)$  are radar backscattering and extinction cross sections ( $\text{mm}^2$ ) of a raindrop with volume equivalent diameter  $D$  ( $\text{mm}$ ) at a wavelength of  $\lambda$  ( $\text{mm}$ ), respectively.

$N(D)$  ( $\text{mm}^{-1}\text{m}^{-3}$ ) is the gamma DSD and expressed as (Ulbrich 1983; Bringi and Chandrasekar 2001)

$$N(D) = N_w f(\mu) \left(\frac{D}{D_m}\right)^\mu \exp(-\Lambda D), \quad (4)$$

where  $N_w$  is a scale factor, and

$$f(\mu) = \frac{6(4+\mu)^{\mu+1}}{4^4 \Gamma(\mu+4)}, \quad (5)$$

and

$$\Lambda = (4 + \mu)/D_m, \quad (6)$$

where  $\Gamma$  is the Gamma function, and  $\mu$  is the shape factor of the gamma distribution.  $D_m$  is the mass-weighted diameter of particle spectra, defined as follows

$$D_m = \frac{\int_{D_{\min}}^{D_{\max}} D^4 N(D) dD}{\int_{D_{\min}}^{D_{\max}} D^3 N(D) dD}, \quad (7)$$

$D_{\min}$  and  $D_{\max}$  are the minimum and maximum diameters of raindrops, respectively. The rain rate is computed by

$$R = 6\pi \times 10^{-4} \int_{D_{\min}}^{D_{\max}} N(D) \cdot D^3 V(D) dD, \quad (8)$$

where  $V(D)$  is raindrop fall velocity and expressed as a function of  $D$ .

Because the radar reflectivity factor usually spans a large range of magnitudes, it is conveniently expressed in decibels (dB) of reflectivity or dBZ as follows

$$Z = 10\log_{10} z. \quad (9)$$

Note that lower  $z$  and upper case  $Z$  denote linear and logarithmic reflectivities, respectively, throughout this study. The radar differential frequency ratio (DFR) in dB is defined as

$$DFR = Z_{Ku} - Z_{Ka}, \quad (10)$$

where  $Z_{Ku}$  (dBZ) and  $Z_{Ka}$  (dBZ) are the radar reflectivity factors at wavelengths of Ku and Ka bands. From (2), (4) and (10) it is not difficult to show that DFR is independent of  $N_w$ . Using (4), Fig.1 shows  $D_m$  (left) and the  $z_{Ku}$ -normalized rain rate (right) as a function of DFR for several  $\mu$  values. Note that the one-to-one relationship between  $D_m$  and DFR when DFR is greater than zero, implying that, if  $\mu$  is known and the DFR is positive,  $D_m$  can be determined uniquely. However, double solutions of  $D_m$  occur as the DFR becomes negative. This has also been found by many earlier studies (Meneghini et al. 1992 and 1997; Mardiana et al. 2004; Liao and Meneghini 2005; Rose and Chandrasekar 2005; Seto et al. 2013; Seto and Iguchi 2015). Similar features are found in the normalized rain rate plots shown in the right panel of Fig.1, where a unique solution to  $R/z_{Ku}$  is available only when the DFR is positive.

The axes of the plots in Fig.2 are the same as in Fig. 1 but in this case, the results, displayed as 2-dimensional probability density functions (PDF), are derived from measured DSDs acquired during the Iowa Flooding Studies (IFloodS), the Integrated Precipitation Validation Experiment (IPHEX) and data from NASA Wallops Flight Facility in Wallops Island, Virginia. For the sake of comparisons with model results, theoretical computations from the gamma DSD model with a fixed  $\mu$  of 3 are given by the white curves. It is worth

mentioning that use of the  $z_{Ku}$ -normalized rain rate, as in Figs.1 and 2, is a convenient and effective way to directly infer rain rate from radar parameters. In particular, given a (positive) DFR and an assumed  $\mu$ , the  $R/z_{Ku}$  is obtained from the curves in the figure; multiplication of the result by  $z_{Ku}$  then provides the rain rate estimate.  $N_w$  is obtained from either Ku- or Ka-band reflectivities along with the derived  $D_m$ . For the scattering computations, the raindrops are prescribed as horizontally oriented oblate spheroids with axis ratios that follow the shape-size relations reported by Thurai et al. (2007). Symmetrical axes of the raindrops are aligned in the vertical direction. The T-matrix method is used to compute the scattering properties of single particles (Mishchenko and Travis 1998). It is important to point out that vast majority of the DSD measurements (nearly 70%), as found in Fig.2, fall into the range where the DFR is negative, which suggests a serious problem for operational retrieval algorithms if the DFR- $D_m$  relations are used. For the GPM DPR whose minimum detectable reflectivities are approximately 12 dB and 17 dB at Ku- and Ka-wavelength, respectively, the percentage of the DSD data with the DFR less than 0 is around 37%.

### 3. Modified dual-wavelength Radar Technique

As discussed above, the standard dual-wavelength algorithm is capable of retrieving two parameters of the DSD and rain rate at each range gate if the fixed- $\mu$  gamma DSD model is assumed and if the DFR is positive along the path. Apart from errors in the DSD model assumed, the most serious problem arises from ambiguities in the DFR- $D_m$  and DFR- $R/z_{Ku}$  relationships when the DFR is negative. To lessen the impact of these ambiguities, a modified DFR, denoted by  $DFR^*$ , is introduced and expressed as

$$DFR^* = Z_{Ku} - \gamma Z_{Ka}, \quad (11)$$



where  $\gamma$  is a scale factor with a value ranging from 0 to 1. The definition of DFR\* in (11) can be viewed as a generalized form of the dual-wavelength ratio which reverts to the single-wavelength  $Z_{Ku}$  when  $\gamma=0$  and to the standard dual-wavelength method when  $\gamma=1$ . For  $\gamma$  greater than 0 but less than 1, the Ka-band radar reflectivity is used but reduced from that in the DFR relation. Unlike the DFR, the DFR\* is dependent on  $N_w$ .

Figure 3 illustrates the DFR\*- $D_m$  relation, derived from the DSD data, as  $\gamma$  takes on different values. The thick black solid lines are the means of the data taken at each point along the horizontal axis. Theoretical computations (blue curves) derived from the gamma DSD model with a fixed  $\mu$  of 3 are plotted for  $N_w$  varying from  $10$  to  $10^5 \text{ mm}^{-1}\text{m}^{-3}$ . For reference, the contours of  $Z_{Ku}$  in dBZ (red curves) are also given in the plots. Shown in the top-left panel is the case for the single Ku-band, i.e.,  $\gamma=0$ , while the results from the standard dual-wavelength technique ( $\gamma=1$ ) are shown in the bottom-right panel. The cases where  $\gamma$  is equal to 0.5 and 0.7 are displayed in the top-right and bottom-left panels, respectively. Several interesting features are revealed in Fig.3; in particular,  $D_m$  has one-to-one relation with DFR\* for all the cases shown except for the case where  $\gamma=1$ . As expected, the DFR\*- $D_m$  relations depend on  $N_w$  if  $\gamma$  is not 1, and the degree of the dependence depends on  $\gamma$ . The strongest dependence of  $N_w$  on these relations occurs at  $\gamma=0$  (Ku-band only), as shown from both the DSD-derived data points and the model computations. Variability in the DFR\*- $D_m$  with respect to  $N_w$  tends to decrease for  $D_m$  greater than 1 mm as  $\gamma$  increases. The DFR\* at  $\gamma=1$ , or the standard DFR, is independent of  $N_w$ . It is worth reiterating that one of the crucial differences between the DFR\* ( $\gamma \neq 1$ ) and the standard DFR is that the former gives a unique solution to  $D_m$  for given  $N_w$  and  $\mu$  while the latter results in double values of  $D_m$  for large amount of the radar measurements. Similar behavior is also found in the rain rate estimates, as depicted in Fig.4. Unique solutions to  $D_m$  and rain rate

from the DFR\* are perhaps the most desirable features from the perspective of radar retrievals, but it comes with the cost of adding the variable  $N_w$  to the equations and leading to an under-constrained retrieval. As one of the goals of the spaceborne radar is to obtain hydrometeor profiles along the radar beam, the rest of the paper is focused on how the modified dual-wavelength technique described above is implemented in the profiling algorithms and how its performance compares with algorithms that rely on the standard dual-wavelength technique.

#### **4. Hydrometeor profile retrieval**

Although the modified dual-wavelength method or DFR\* shows potential to improve accuracy of radar estimates over the standard DFR in terms of the uncertainties associated with double solutions, a physical evaluation of the hydrometeor profiling retrieval is required not only for understanding the uncertainties but also in gaining insight into ways to improve the retrievals. To achieve this, the measured DSD data acquired from a variety of storm systems during the NASA field campaigns are used to construct realistic hydrometeor profiles. Using measured DSD spectra both radar and hydrometeor's parameters, which include true and measured radar reflectivities, attenuation, rain and DSD characteristic parameters ( $D_m$  and  $N_w$ ), can be computed. These DSD-calculated parameters then serve as truth. An evaluation of algorithm performances is actually conducted by comparing the radar estimates with the truth. Before showing the results on the DFR\* profiling algorithm performance, we will first describe the radar and hydrometeor profiles simulated by using measured DSD, and then detail the procedures of the DFR\* profile algorithms.

##### **4.1 DSD profiles**

For simplicity but without losing generality, two types of vertical DSD profiles are created: One type is the vertically uniform DSD profile where a single DSD spectrum is used for

entire column, and second type is the non-uniform profile in which the DSD changes gate by gate along the column. The DSD data used in this study are primarily from measurements made by Parsivel disdrometers during the Iowa Flood Studies (IFloodS) field experiment from May 1 to June 15, 2013, the Integrated Precipitation Validation Experiment (IPHEX) from May 1 to June 15, 2014, and the observations at the NASA Wallops Flight Facility in Wallops Island, Virginia from 2013 to 2014. The Parsivel disdrometers are used to measure rain DSD, and fall-velocities of particle sizes from 0.3 to 20 mm.

Shown in Fig.5 is an example of the simulated Ku-band radar reflectivities (top panels) and rain rates (bottom panels) from a segment of 200 DSD vertically uniform (left column) and non-uniform (right column) profiles. The range resolution is 0.125 km, which is comparable to the case for the GPM DPR, with the rain height set at 5 km. To construct realistic non-uniform hydrometeor profiles, the time-series DSD data are converted to vertical profiles by assigning 1-minute-integration-time DSD data to the gates from the top to surface consecutively. The mean values of the correlations of rain,  $D_m$  and  $\log_{10}N_w$  over entire simulated non-uniform profiles between the range gates considered to the surface gate, are plotted in Fig.6 for the cases in which rain rate is less than 5 mm/h (left), greater than 5 mm/h (middle) and greater than zero (right), which approximately represent the stratiform, convective and stratiform-convective-combined rain systems. These correlations are found to be comparable to the results reported by Adirosi et al. (2016) based on a combined study of Micro Rain Radar (MRR) and DSD measurements.

#### 4.2 Modified DFR profiling algorithms

As shown in Fig.3,  $D_m$  can be obtained from  $DFR^*$  if  $N_w$  is known. Likewise, rain rate can be derived if  $DFR^*$  is used along with  $Z_{Ku}$ , as shown in Fig.4. These procedures for the retrieval of  $D_m$  and rain rate constitute the basis for the  $DFR^*$ -based profiling algorithms. On the other

hand, the Ku- and Ka-band radar signals undergo losses caused by attenuation of the signals out to the gate at which the radar measurements are made. Accurate attenuation correction is therefore important for the algorithm's overall performance. For down-looking air/space-borne radar, forward and backward recursive procedures are often used for attenuation correction. In the forward approach, the retrieval starts from storm top and then proceeds into storm gate by gate until reaching the surface or final clutter-free gate. Conversely, the backward approach begins at the surface with a known PIA that is usually estimated by the surface reference technique (SRT) or other independent measurements (such as radiometers), with the correction moving upward until reaching the storm top. Benefits and demerits of the forward and backward approaches depend on the types of error sources involved in the algorithms. Nevertheless, it is clear that uncertainties associated with PIA only affect the performance of the backward recursive method while errors associated with attenuation corrections prior to rain, such as attenuation resulting from cloud water and the melting region, are directly related to the performance of the forward recursive method.

To retrieve rain and DSD profiles using DFR\*, one simple way is to assign the same  $N_w$  to each range gate of one vertical profile as an initialization process. With a known  $N_w$ ,  $D_m$  can be uniquely derived from the DFR\* if a fixed  $\mu$  is assumed; rain rate and attenuation coefficients can then be derived by using DFR\* along with  $Z_{Ku}$ . Attenuation corrections to the measured radar reflectivity profiles are carried out consecutively gate-by-gate along the radar beam either in the forward or backward direction. Since the derived hydrometeor profiles depend on the value of  $N_w$  assumed, finding the proper  $N_w$  that leads to accurate DSD and rain profiles is a key to the retrieval procedure.

In the search for  $N_w$ , an optimization method is employed to minimize the discrepancies between the simulated and measured radar parameters. Following Seto et al. (2016)  $N_w$  is selected to maximize the product of the following three probability functions (or constraints) from the computations conducted by using a series of initial values of  $N_w$ , denoted by  $\tilde{N}_{w,k}$ , where  $k=1, 2, \dots, K$  (where  $K$  is the total number of the initial tests of  $N_w$ ),

$$p_1(N_w)p_2(N_w)p_3(N_w) = \max(p_1(\tilde{N}_{w,k})p_2(\tilde{N}_{w,k})p_3(\tilde{N}_{w,k})), \quad (12)$$

where

$$p_1(\tilde{N}_{w,k}) = \frac{1}{\sigma_1\sqrt{2\pi}} \exp\left(-\frac{(\log_{10}\tilde{N}_{w,k}-3.45)^2}{2\sigma_1^2}\right), \quad (13)$$

$$p_2(\tilde{N}_{w,k}) = \frac{1}{\sqrt{2\pi}} \exp\left(-\frac{(\delta PIA(\tilde{N}_{w,k})-\delta PIA_{SRT})^2}{2\sigma_2^2}\right), \quad (14)$$

$$p_3(\tilde{N}_{w,k}) = \prod_{n=1}^N \frac{1}{\sqrt{2\pi}} \exp\left(-\frac{(Z_{m,n,est}^{(Ka)}(\tilde{N}_{w,k})-Z_{m,n,obs}^{(Ka)})^2}{2N\sigma_3^2}\right), \quad (15)$$

where  $N$  is the number of range gates along the column, and  $\delta PIA$  is the differential PIA over the full column defined as difference of PIA between Ka- and Ku-band.  $Z_{m,n,est}^{(Ka)}(\tilde{N}_{w,k})$  and  $Z_{m,n,obs}^{(Ka)}$  are respectively the simulated and measured Ka-band apparent radar reflectivities at the  $n$ th range gate. The function  $p_1(\tilde{N}_{w,k})$  describes the distribution of  $\log_{10}(N_w)$  that has a mean of 3.45 in  $\log_{10}(\text{mm}^{-1}\text{m}^{-3})$  and a standard deviation  $\sigma_1$ , derived from the DSD data.  $p_2(\tilde{N}_{w,k})$  is associated with the difference in  $\delta PIA$  between the DSD-estimated value and the SRT estimate while  $p_3(\tilde{N}_{w,k})$  accounts for discrepancies between the simulated and measured Ka-band reflectivities. Note that  $(\sigma_2)^2$  is the error variance associated with the SRT estimate of the differential path attenuation. The term  $\sigma_3$  is a constant that determines weighting of measurements of the Ka-band reflectivities in the overall constraint. The smaller this value is, the more the Ka-band measurements are weighted. It is worth mentioning that the reason that  $\delta PIA$

is used rather than the PIA at either or both wavelengths is that the former usually has a smaller error variance than the latter if they are estimated by the SRT because of strong correlation of the normalized surface cross section ( $\sigma^0$ ) between Ku- and Ka-band (Meneghini et al. 2015). It is also worth noting that optimization is not required in the standard method since in this case, the DFR is used to estimate  $D_m$  directly;  $N_w$  is then found from  $D_m$  and  $Z_{Ku}$  or  $Z_{Ka}$ .

More detail on the optimization described above is given by the flowchart in Fig.7 which shows the gate-by-gate progression of the retrieval from the rain top to the surface (forward approach). The procedure starts with equally-spaced values of  $\log_{10}(\tilde{N}_{w,k})$  ( $k=1, 2, \dots, K$ , where  $K=100$ ) in the range from 0 to 6, from which the radar and hydrometeor profiles are estimated. The procedure is repeated  $K$  times, and the final  $N_w$  is chosen as the value that maximizes (12). Once  $N_w$  is selected, profiles of  $D_m$  and rain rate are found from look-up tables (LUT) that express  $D_m$  as a function of  $N_w$  and  $DFR^*(\gamma)$ . Accumulated Ku- and Ka-band attenuations ( $A_{Ku}$  and  $A_{Ka}$  in dB) are computed from the specific attenuations ( $k_{Ku}$  and  $k_{Ka}$  in dB/km) of previous gates. The backward approach is done in the same fashion. Unlike the forward approach where the retrieval starts at the rain top where the attenuation is assumed to be negligible, the backward approach begins at the gate near surface where the SRT-derived PIAs are used to estimate the attenuation-corrected reflectivities from the measured radar reflectivities. The backward retrievals are therefore dependent on the accuracy of the PIA estimate.

## 5. Evaluation of DFR\* Algorithms

Assessments of the modified DFR performance in estimates of rain and  $D_m$  are conducted by comparing the estimated results with the true values that are obtained from direct computations from the simulated DSD profiles. Figures 8 and 9 depict, in terms of 2-dimensional probability density functions, the comparisons of  $D_m$  and rain rates derived from the modified-

1 DFR with  $\gamma=0$  and 0.7 (left and middle columns) and the standard DFR (right columns) to the  
 2 corresponding true values of  $D_m$  and  $R$ . The forward recursive approach, as described in Fig.7,  
 3 is applied to the non-uniform DSD profiles that are prescribed earlier for these retrievals. To  
 4 track the statistical errors along the profiles, the comparisons are made at the rain top and the  
 5 surface that correspond to the beginning and end of the profiles. An unbiased  $\delta$ PIA model with  
 6 the standard deviation of 0.8 dB, which is similar to what has been found from the GPM DPR  
 7 measurements over ocean, is used to characterize the PIA errors. The  $\sigma_1$ ,  $\sigma_2$  and  $\sigma_3$  in (13)-(15)  
 8 are 3.45 in  $\log_{10}(\text{mm}^{-1}\text{m}^{-3})$ , 1.6 in dB (two times of the standard deviation of  $\delta$ PIA) and 2 in dBZ,  
 9 respectively. Choice of these values seems to lead reasonable and robust estimates after  
 10 extensive tests. For the standard DFR method, when negative DFR occurs, the larger of the two  
 11  $D_m$  solutions is chosen. To be consistent with the GPM DPR, the DSD data are used only if the  
 12 DSD-computed Ku-band reflectivities are greater than 12 dBZ and the Ka-band reflectivities  
 13 greater than 17 dBZ (DPR sensitivity thresholds). Comparisons of the results derived from the  
 14 modified and standard DFR methods clearly indicate that the modified DFR delivers far more  
 15 accurate estimates than does the standard DFR for both rain rate and  $D_m$ . The results show  
 16 generally good correlations between the modified-DFR estimates and the true values despite a  
 17 slight degradation in accuracy as the retrieval progresses down to the surface. This degradation  
 18 is the result of accumulating errors in the attenuation correction for ranges deeper into the storm.  
 19 The rain estimates are more accurate than the  $D_m$  estimates because retrieval of  $D_m$  is more  
 20 sensitive to the DSD model assumed, such as selection of  $\mu$  for the gamma distribution, than is  
 21 the rain retrieval. It is noticed that there are only slight differences of  $R$  and  $D_m$  estimates  
 22 between the  $\gamma$  values of 0 and 0.7. This is because the non-uniform DSD profiles presented in  
 23 this study don't actually result in significantly large variations of  $N_w$  in the profiles. For the case

1 of relatively highly uncorrelated DSD profile, in which the differences in the estimates between  
2  $\gamma=0$  and  $\gamma=0.7$  are clearly noticeable, i.e., the estimates at  $\gamma=0.7$  appear less variable than those at  
3  $\gamma=0$  (not shown).

4 As expected, larger uncertainties in the estimates of rain and  $D_m$  using the standard DFR  
5 take place when the double values occur, as shown in the top-right panels of Figs. 8 and 9. These  
6 errors, however, tend to decrease as  $D_m$  or rain rate become large; that is, when the DFR- $D_m$   
7 relationship is single-valued. The ambiguities associated with the double solutions not only  
8 adversely affect the retrievals of rain rate and  $D_m$  but also introduce errors into the attenuation  
9 corrections. This effect can be seen in the bottom-right panels of Figs.8 and 9 where errors  
10 associated with the Ku- and Ka-band attenuation corrections become severe enough at the  
11 surface to strongly degrade the retrieval estimates, particularly estimates of  $D_m$ . The modified  
12 and standard DFR comparisons also have been made at the intermediate gates (not shown).  
13 These profiles at intermediate gates behave similarly to those in Figs.8 and 9 and are bounded by  
14 the results estimated at the beginning and end of the profiles.

15 Figs.10 and 11 show the same retrieval results as in Figs.8 and 9 but for the backward  
16 approach. The general behavior of the results obtained from the backward approach largely  
17 remains the same as that obtained from the forward approach. Like the forward approach, the  
18 modified DFR is superior to the standard DFR method. Because of a reversal of direction of the  
19 solution, the last gate of the backward method terminates at the rain top at which the path  
20 attenuations from radar are generally small. Unlike the forward method, the accuracy of the PIAs  
21 plays a crucial role for the overall performance of the backward procedure.

22 For the results shown in Figs.8-11 the DSDs along the vertical column are taken to be non-  
23 uniform, i.e., partially correlated along the column. If the DSDs are assumed to be fully



correlated instead of partially correlated, the rain rate and  $D_m$  estimates from the modified DFR tend to improve (not shown). This improvement is the result of the fact that fully correlated DSDs are consistent with the assumption that  $N_w$  is constant over the full profile. Changes in  $\sigma_1$ ,  $\sigma_2$  and  $\sigma_3$  values modify the details of the retrievals but not the general characteristics of the results. The functions  $p_1$ ,  $p_2$  and  $p_3$  of (13)-(15), serving as constraints on the solutions, play various roles in constraining the results, and their impact on the solutions change with rain intensity. For example,  $p_1$  constitutes a fairly strong constraint in finding the solutions throughout entire rain rate range.  $p_2$  is a weak constraint for rain less than 1 mm/h, a moderate constraint for rain rates between 1 and 10 mm/h, and a strong constraint for rain rates greater than 10 mm/h.  $p_3$  functions in a manner quite similar to  $p_2$  in the sense that it is a strong constraint at moderate and heavy rains, and is a slightly stronger constraint than  $p_2$  for light rain. Overall, the combination of  $p_1$ ,  $p_2$  and  $p_3$  provide stronger constraints to the retrieval at moderate-heavy rain rates than for light rain. This is because relative errors of  $\delta PIA$  (in  $p_2$  or (13)) become large for the cases where the PIAs are small, which are often associated with the light rain. The Ka-band radar does not provide much additional information if the rain rate is light. In these cases, the backscattering at both Ku- and Ka-band is primarily Rayleigh and the second frequency adds little additional information.

## 6. Summary and remarks

Development of a realistic and physically based framework to evaluate dual-wavelength radar techniques from space is important in assessing the accuracy of current and future retrieval algorithms for the dual-wavelength algorithms. In this study we employ measured DSD data from various NASA-sponsored field campaigns to construct vertical DSD profiles. With these profiles the measured and attenuation-corrected radar reflectivity factors are simulated along

1 with the corresponding rain rate and DSD parameters. The simulated radar reflectivities and  
2 hydrometeor parameters, because they are directly computed from the measured DSD, are  
3 considered as truth. Evaluation of the retrieval algorithms is conducted by comparing the  
4 hydrometeor parameters derived from the algorithms that use the DSD-simulated measured  
5 reflectivities as inputs with those directly computed from the DSD profiles. For the radar  
6 simulations the effect of radar random error and calibration bias are not taken into account.

7 The standard dual-wavelength technique, which relies on DFR- $D_m$  relations, has long been  
8 considered as a possible means to derive rain and DSD parameters. However, for the Ku and Ka  
9 combination, negative values of DFR lead to ambiguities in the estimation of  $D_m$  that can result  
10 in large uncertainties in the rain and DSD estimates. If the forward approach is employed, these  
11 uncertainties grow larger as the retrieval proceeds deep into the storm as errors are accumulated  
12 along the retrieval direction. In an attempt to circumvent the ambiguities in the  $D_m$  estimation  
13 that the standard dual-wavelength method faces, we introduce a modified version of the standard  
14 technique, i.e., the modified dual-wavelength technique, which partially weights the Ka-band  
15 measurements in the radar differential-frequency-ratio equations. The modified DFR or DFR\*  
16 can be viewed as the generalized version of the DFR, from which the standard DFR and the  
17 single Ku-band equations are the extreme cases with weighting factors of 1 and 0, respectively.

18 It has been shown that the modified DFR has a unique relation with  $D_m$  if the weighting  
19 factor (or  $\gamma$ ) is less than 0.8 for a given  $N_w$ . Unlike the standard DFR (where  $\gamma=1$ ), the DFR\*- $D_m$   
20 relations are dependent on  $N_w$ . The degree to which the DFR\* depends on  $N_w$  depends in turn on  
21 the value of  $\gamma$ . Generally speaking, dependence of the DFR\*- $D_m$  on  $N_w$  tends to become weaker  
22 as  $\gamma$  increases. From the perspective of radar retrieval, the strategy is to choose as large a  $\gamma$  as  
23 possible as long as a unique solution of  $D_m$  is achievable. However, a choice of  $\gamma$  near 1 leads to

1 an abrupt transition (non-linear behavior) in the  $DFR^*-D_m$  relations in the range where  $D_m$  is less  
2 than 1, causing unstable solutions at small values of  $D_m$ . Appropriate choice of  $\gamma$  will also  
3 depend on some other factors, such as non-uniformity of hydrometeor profiles and model  
4 assumptions.

5 To apply the modified DFR for the retrieval of rain profiles, following the work of Seto et  
6 al. (2016), an optimal profiling retrieval algorithm is first described and then evaluated using the  
7 simulated DSD profiles. This is a recursive procedure that infers hydrometeor parameters and  
8 makes attenuation correction gate-by-gate along either forward (storm top, towards the surface)  
9 or backward (surface, towards the storm top) along the radar beam. As our primary focus is on  
10 examining the mechanics of rain retrieval techniques and assessing their retrieval errors, the  
11 uncertainties associated with cloud water and melting hydrometeors that often appear atop the  
12 rain as well as the issues related to non-uniform beam filling (NUBF) and multiple scattering are  
13 excluded in our evaluation. As such, the attenuation at the first gate for the forward approach  
14 (rain top), the gate where the retrieval starts, is assumed to be zero. The PIA is used as the  
15 attenuation of the first gate for the backward approach, which is the range gate closest to the  
16 surface. The  $DFR^*$ -based retrievals are carried out  $K$  times for a given DSD profile in  
17 correspondence with the  $K$  equally-spaced initialized  $\log_{10}(N_w)$ . The final  $N_w$  is then determined  
18 as that value that maximizes the product of three probability functions that minimize the  
19 differences between the radar measurements and the estimates. Once  $N_w$  is fixed, the range-  
20 profiled rain rate and  $D_m$  are derived.

21 It should be pointed out that constant  $N_w$  along the vertical profile is an approximation,  
22 which is true only if the vertical DSD is uniform. For non-uniform DSD profiles, such as the  
23 cases studied in the paper,  $N_w$  varies from gate to gate. The constant  $N_w$  approximation leads to

errors but these errors are limited by the fact that the natural vertical variations in the DSD are not too strong and the fact that the retrieved  $N_w$  will be close to a weighted mean of the actual  $N_w$  values along the path.

Comparisons of the estimates of the rain rate and  $D_m$  obtained from the modified and standard DFR to the true values indicate that the DFR\*-based profiling retrievals are superior to those from the standard DFR. This is true for both forward and backward approaches. As mentioned earlier, attenuations caused by melting layer and cloud water are not included in our evaluation framework, and errors associated with these attenuations are not taken into account. These errors, if considered, will lead to performance degradation for the forward approach but not for the backward method. The backward approach, however, depends on the accuracy of PIA. Highly unreliable PIA will degrade its performance. It is necessary to point out that for the snow retrieval in which the DFR usually has a unique relation to  $D_m$  from the Ku- and Ka-band radar, the standard technique is often advantageous over other approaches because it fully accounts for the particle size distribution (PSD) variations in space and time. This is probably true for other frequency pairs that exhibit either a unique DFR- $D_m$  relation or much-reduced region of DFR where the double solutions occur.

The benefits of introducing the DFR\* are twofold: varying  $\gamma$  from 0 to 1 coincides with a transition from the single frequency case to the full dual-frequency case; the double-valued solutions obtained when  $\gamma=1$  can be mitigated by decreasing  $\gamma$ . Although the DFR\* with  $\gamma<1$  introduces dependency on  $N_w$ , it facilitates the use of optimal estimation methods similar to that used in the DPR operational retrieval method. Seeking the most reliable and accurate optimization method, though not the main purpose of this study, is important and will therefore be pursued in future studies.

1  
2 **ACKNOWLEDGEMENTS:** This work is supported by Dr. R. Kakar of NASA Headquarters  
3 under NASA's Precipitation Measurement Mission (PMM) Grant NNH15ZDA001N-PMM. The  
4 authors also wish to thank Dr. Ali Tokay from University of Maryland Baltimore County for  
5 providing DSD data.

## References

- Adirosi, E., L. Baldini, N. Roberto, P. Gatlin, and A. Tokay. 2016. "Improvement of vertical profiles of raindrop size distribution from micro rain radar using 2D video disdrometer measurements." *Atmospheric Research*, **169**, 404-415.
- Bringi, V. N., and V. Chandrasekar, 2001: *Polarimetric Doppler Weather Radar –Principles and Applications*. Cambridge University Press, 664 pp.
- Bringi, V., G. Huang, V. Chandrasekar and E. Gorgucci, 2002: A methodology for estimating the parameters of a Gamma raindrop size distribution model from polarimetric radar data: Application to a squall-line event from the TRMM/Brazil campaign. *J. Oceanic and Atmos. Tech.*, **19**, 633-645.
- Feingold, G., and Z. Levin, 1986: The lognormal fit to raindrop spectra from frontal convective clouds in Israel. *J. Appl. Meteor.*, **25**, 1346–1363.
- Gorgucci, G. Scarchilli, V. Chandrasekar and V. Bringi, 2000: Measurement of mean raindrop shape from polarimetric radar observations. *J. Atmos. Sci.*, **57**, 3406-3413.
- Gorgucci, E., G. Scarchilli, V. Chandrasekar, and V. Bringi, 2002: Estimation of raindrop size distribution parameters from polarimetric radar measurements. *J. Atmos. Sci.*, **59**, 2373-2384.
- Hou A., Y., R. K. Kakar, S. Neeck, A. A. Azarbarzin, C. D. Kummerow, M. Kojima, R. Oki, K. Nakamura, and T. Iguchi, 2014: The global precipitation measurement mission. *Bull. American Meteor. Soc.*, **95**, pp. 701-722.
- Grecu, M., L. Tian, W. S. Olson, and S. Tanelli, 2011: A robust dual frequency radar profiling algorithm. *J. Appl. Meteor. Climatol.*, **50**, 1543–1557.

1 Liao, L., and R. Meneghini, 2005: A study of air/space-borne dual-wavelength radar for  
2 estimates of rain profiles. *Advances in Atmospheric Sciences*, **22**, 841-851.

3 Liao, L., R. Meneghini, A. Tokay, and L. F. Bliven, 2016: Retrieval of snow properties for Ku-  
4 and Ka-band dual-frequency radar. *J. Appl. Meteor. Climatol.*, **55**, 1845-1858.

5 Mardiana, R., T. Iguchi, and N. Takahashi, 2004: A dual-frequency rain profiling method  
6 without the use of a surface reference technique. *IEEE Trans. Geosci. Remote Sens.*, **42**,  
7 2214-2225.

8 Mishchenko, M. I., and L. D. Travis, 1998: Capabilities and limitations of a current FORTRAN  
9 implementation of the T-matrix method for randomly oriented, rotation symmetric scatterers.  
10 *J. Quan. Spec. Rad. Transfer*, **60**, 309-324.

11 Meneghini, R., T. Kozu, H. Kumagai, and W.C. Boncyk, 1992: A study of rain estimation methods  
12 from space using dual-wavelength radar measurements at near-nadir incidence over ocean, *J.*  
13 *Atmos. Oceanic Technol.*, **9**, pp. 364-382.

14 Meneghini, R., H. Kumagai, J. R. Wang, T. Iguchi, and T. Kozu, 1997: Microphysical retrievals  
15 over stratiform rain using measurements from an airborne dual-wavelength radar radiometer.  
16 *IEEE Trans. Geosci. Remote Sens.*, **35**, 487-506.

17 Meneghini, R., H. Kim, L. Liao, and J. A. Jones, and J. M. Kwiatkowski, 2015: An initial  
18 assessment of the Surface Reference Technique applied to data from the Dual-Frequency  
19 Precipitation Radar (DPR) on the GPM Satellite. *J. Atmos. Oceanic Technol.*, **32**, 2281-2296.

20 Rose, C. R. and V. Chandrasekar, 2005: A system approach to GPM Dual-frequency retrieval.  
21 *IEEE Trans. Geosci. Remote Sens.*, **43**, 1816-1826

1 Seto S., T. Iguchi and T. Oki, 2013: The basic performance of a precipitation retrieval algorithm  
2 for the Global Precipitation Measurement mission's single/dual frequency radar  
3 measurements. *IEEE Trans. Geosci. Remote Sens.*, **51**, 5239–5251.

4 Seto, S., and T. Iguchi, 2015: Intercomparison of attenuation correction methods for the GPM  
5 dual-frequency precipitation radar. *J. Atmos. Oceanic Technol.*, **32**, 915-926.

6 Seto, S., T. Shimosuma, T. Iguchi and T. Kozu, 2016: Spatial and temporal variations of  
7 mass-weighted mean diameter estimated by GPM/DPR. *2016 IEEE International*  
8 *Geoscience and Remote Sensing Symposium (IGARSS)*, Beijing, 3938-3940. doi:  
9 10.1109/IGARSS.2016.7730023.

10 Thurai, M., G. J. Huang, V. N. Bringi, W. L. Randeu, and M. Schönhuber, 2007: Drop shapes,  
11 model comparisons, and calculations of polarimetric radar parameters in rain. *J. Atmos*  
12 *Oceanic Technol.*, **24**, 1019-1032.

13 Ulbrich, C. W., 1983: Natural variations in the analytical form of the raindrop size distribution.  
14 *J. Appl. Meteor. Climatol.*, **22**, 1764-1775.



## Figure Captions:

Fig.1 Computational results of  $D_m$  vs. DFR (left) and  $z_{Ku}$ -normalized rain rate vs. DFR (right) as the gamma DSD model is assumed with  $\mu$  values of 0, 3, 6 and 10.

Fig.2 Two-dimensional probability density functions, as derived from the DSD measurements taken during several NASA field campaigns, between  $D_m$  and DFR (left) and  $z_{Ku}$ -normalized rain rate vs. DFR (right). Theoretical computations from the gamma DSD model of  $\mu=3$  are also plotted as references.

Fig.3 Scatterplots of  $D_m$  versus modified DFR as derived from the DSD data for the cases of the weighting factor  $\gamma$  of the modified DFR equal to 0, 0.5, 0.7 and 1. Colors of the data points depict  $N_w$  values that are derived from the same DSD data. The mean values of the data are given by the thick dark curves. Theoretical model computations, represented by blue and red curves, are provided as the DSD is modeled as the gamma distributions with a fixed  $\mu$  of 3 and  $N_w$  (blue curves) ranging from  $10$  to  $10^5$  in  $\text{mm}^{-1}\text{m}^{-3}$ . Contours of  $Z_{Ku}$  at the values from 0 to 40 dB (red curves) are plotted as well for reference.

Fig.4 Scatterplots of  $Z_{Ku}$ -normalized rain rate versus modified DFR as derived from the DSD data for the cases of the weighting factor  $\gamma$  of the modified DFR equal to 0, 0.5, 0.7 and 1. Colors of the data points depict  $N_w$  values derived from the same DSD data. The mean values of the data are given by the thick dark curves. Theoretical model computations, represented by blue and red curves, are provided as the DSD is modeled as the gamma distributions with a fixed  $\mu$  of 3 and  $N_w$  ranging from  $10$  to  $10^5$  in  $\text{mm}^{-1}\text{m}^{-3}$ . Contours of  $Z_{Ku}$  at the values from 0 to 40 dB (red curves) are plotted as well for reference.

Fig.5 Ku-band radar reflectivities (top panels) and rain rate (bottom panels) simulated from a segment of the DSD profiles generated from measured DSD data. Homogeneously vertical DSD profiles are given in the left column while the non-uniform DSD profiles are provided in the right column.

Fig.6 Averaged spatial correlations of rain rate,  $D_m$  and  $\log_{10}N_w$  for the non-uniform DSD profiles between radar range heights and surface. Results from three rain ranges, i.e.,  $R<5$ ,  $R\geq 5$  and  $R>0$  mm/h (all rain), are provided for approximately representing stratiform, convective and their combined systems.

Fig.7 Flowchart of the modified dual-wavelength technique (DFR\*) for retrieval of DSD parameters and rain rate. Outer-loop variable  $k$  goes from 1 to  $K$  to provide equal-spaced values of  $\log_{10}(\tilde{N}_{w,k})$  at each step while inner-loop variable  $n$ , running from 1 to  $N$ , represents radar range gates at which the retrievals are carried out.

Fig.8 Two-dimensional probability density functions of  $D_m$  estimated by the modified DFR with  $\gamma$  of 0 and 0.7 (left and middle columns) as well as the standard DFR ( $\gamma=1$ ) (right column) with the true  $D_m$  for the range gate at the rain top (top row) and at the surface (bottom row). The one-to-one lines are given by the black solid curves while the means and twice the standard

1 deviations of the data are given by the white solid curves and vertical bars, respectively. For  
2 both the modified and standard DFR methods, the forward recursive approach is used and  
3 applied to the non-uniform DSD profiles. An unbiased statistical  $\delta$ PIA model with the standard  
4 deviation of 0.8 dB is assumed.

5  
6 Fig.9 Two-dimensional probability density functions of rain rate estimated by the modified  
7 DFR with  $\gamma$  of 0 and 0.7 (left and middle columns) as well as the standard DFR ( $\gamma=1$ ) (right  
8 column) with the true rain rate for a range gate at the rain top (top row) and at the surface  
9 (bottom row). The one-to-one lines are given by the black solid curves while the means and  
10 twice the standard deviations of the data are given by the white solid curves and vertical bars,  
11 respectively. The non-uniform DSD profiles are assumed and the forward recursive approach is  
12 applied for both the standard and modified DFR methods. An unbiased statistical  $\delta$ PIA model  
13 with the standard deviation of 0.8 dB is assumed.

14  
15 Fig.10 Two-dimensional probability density functions of  $D_m$  estimated by the modified DFR  
16 with  $\gamma$  of 0 and 0.7 (left and middle columns) as well as the standard DFR ( $\gamma=1$ ) (right column)  
17 with the true  $D_m$  for a range gate at the rain top (top row) and at the surface (bottom row). The  
18 one-to-one lines are given by the black solid curves while the means and twice the standard  
19 deviations of the data are given by the white solid curves and vertical bars, respectively. The  
20 backward recursive approach is applied in all cases to the non-uniform DSD profiles. Unbiased  
21 statistical PIA and  $\delta$ PIA models with the standard deviations of 2 dB and 0.8 dB are assumed,  
22 respectively.

23  
24 Fig.11 Two-dimensional probability density functions of rain rate estimated by the modified  
25 DFR with  $\gamma$  of 0 and 0.7 (left and middle columns) as well as the standard DFR ( $\gamma=1$ ) (right  
26 column) with the true rain rate for a range gate at the rain top (top row) and at the surface  
27 (bottom row). The one-to-one lines are given by the black solid curves while the means and  
28 twice the standard deviations of the data are given by the white solid curves and vertical bars,  
29 respectively. The backward recursive approach is applied to the non-uniform DSD profiles.  
30 Unbiased statistical PIA and  $\delta$ PIA statistical models with the standard deviations of 2 dB and 0.8  
31 dB are assumed, respectively.  
32

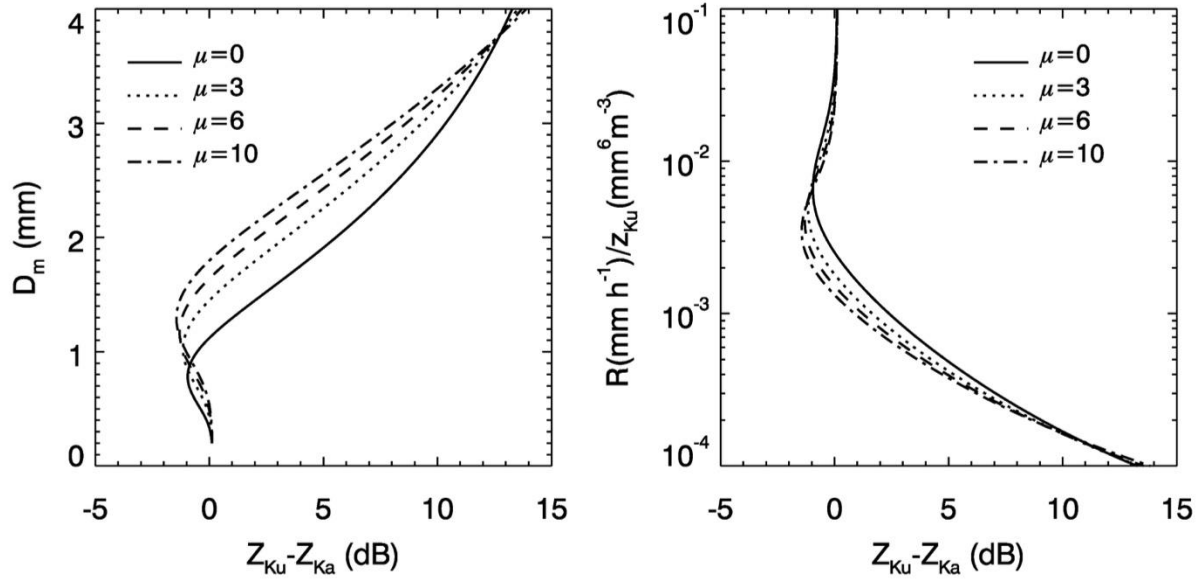


Fig.1 Computational results of  $D_m$  vs. DFR (left) and  $Z_{Ku}$ -normalized rain rate vs. DFR (right) as the gamma DSD model is assumed with  $\mu$  values of 0, 3, 6 and 10.

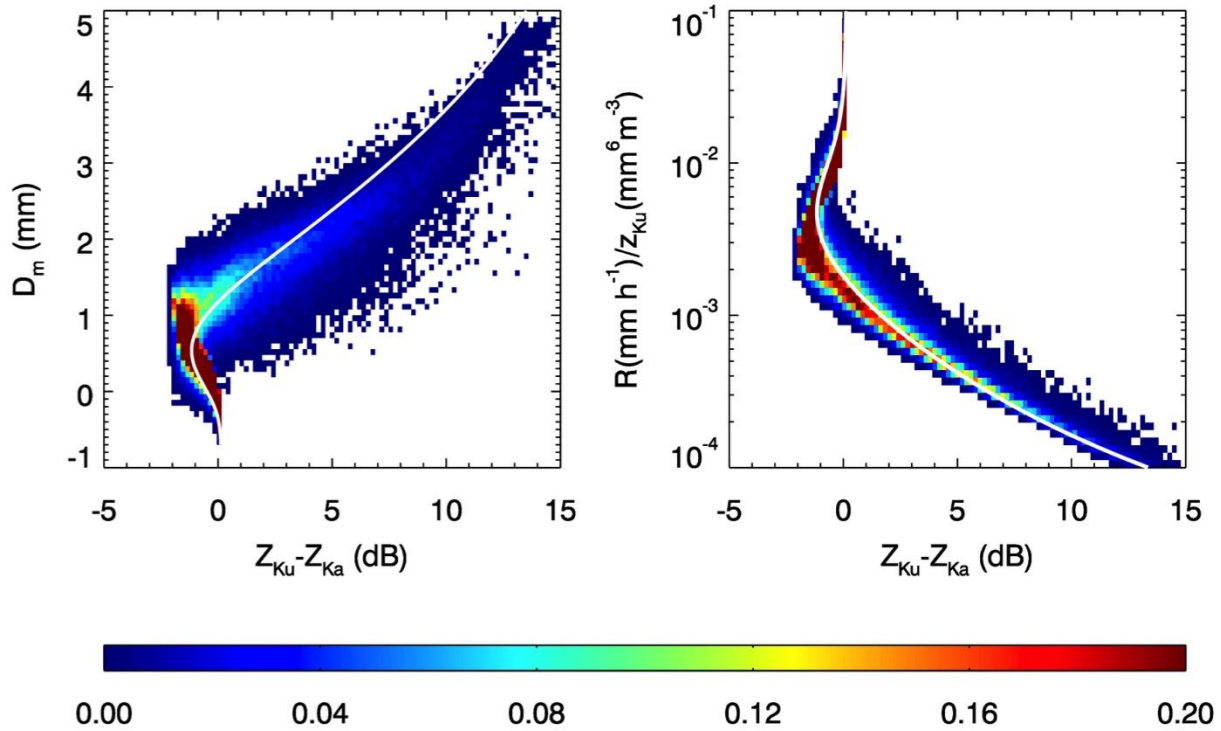


Fig.2 Two-dimensional probability density functions, as derived from the DSD measurements taken during several NASA field campaigns, between  $D_m$  and DFR (left) and  $Z_{Ku}$ -normalized rain rate vs. DFR (right). Theoretical computations from the gamma DSD model of  $\mu=3$  are also plotted as references.

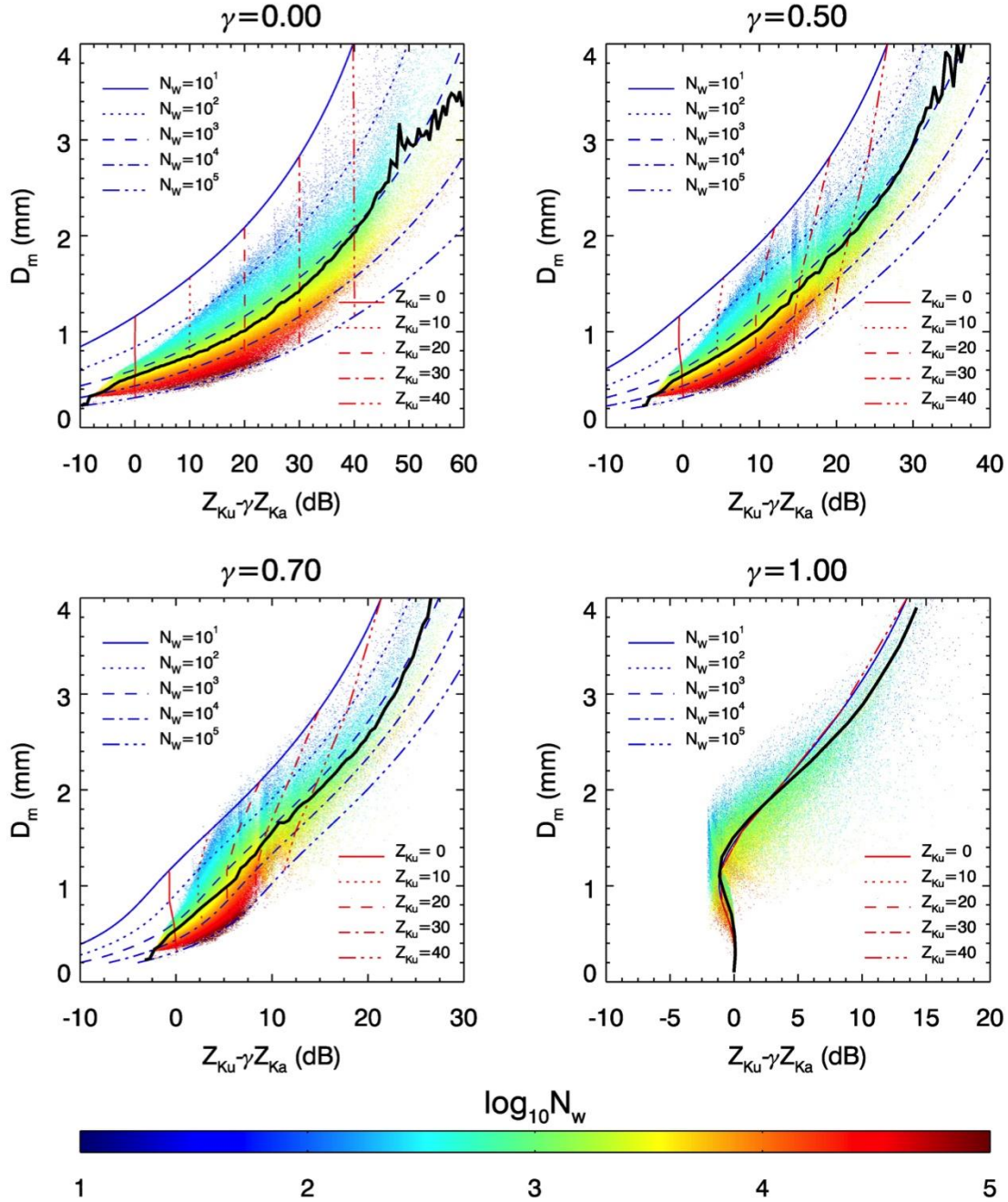


Fig.3 Scatterplots of  $D_m$  versus modified DFR as derived from the DSD data for the cases of the weighting factor  $\gamma$  of the modified DFR equal to 0, 0.5, 0.7 and 1. Colors of the data points depict  $N_w$  values that are derived from the same DSD data. The mean values of the data are given by the thick dark curves. Theoretical model computations, represented by blue and red curves, are provided as the DSD is modeled as the gamma distributions with a fixed  $\mu$  of 3 and  $N_w$  (blue curves) ranging from  $10$  to  $10^5$  in  $\text{mm}^{-1}\text{m}^{-3}$ . Contours of  $Z_{Ku}$  at the values from 0 to 40 dB (red curves) are plotted as well for reference.

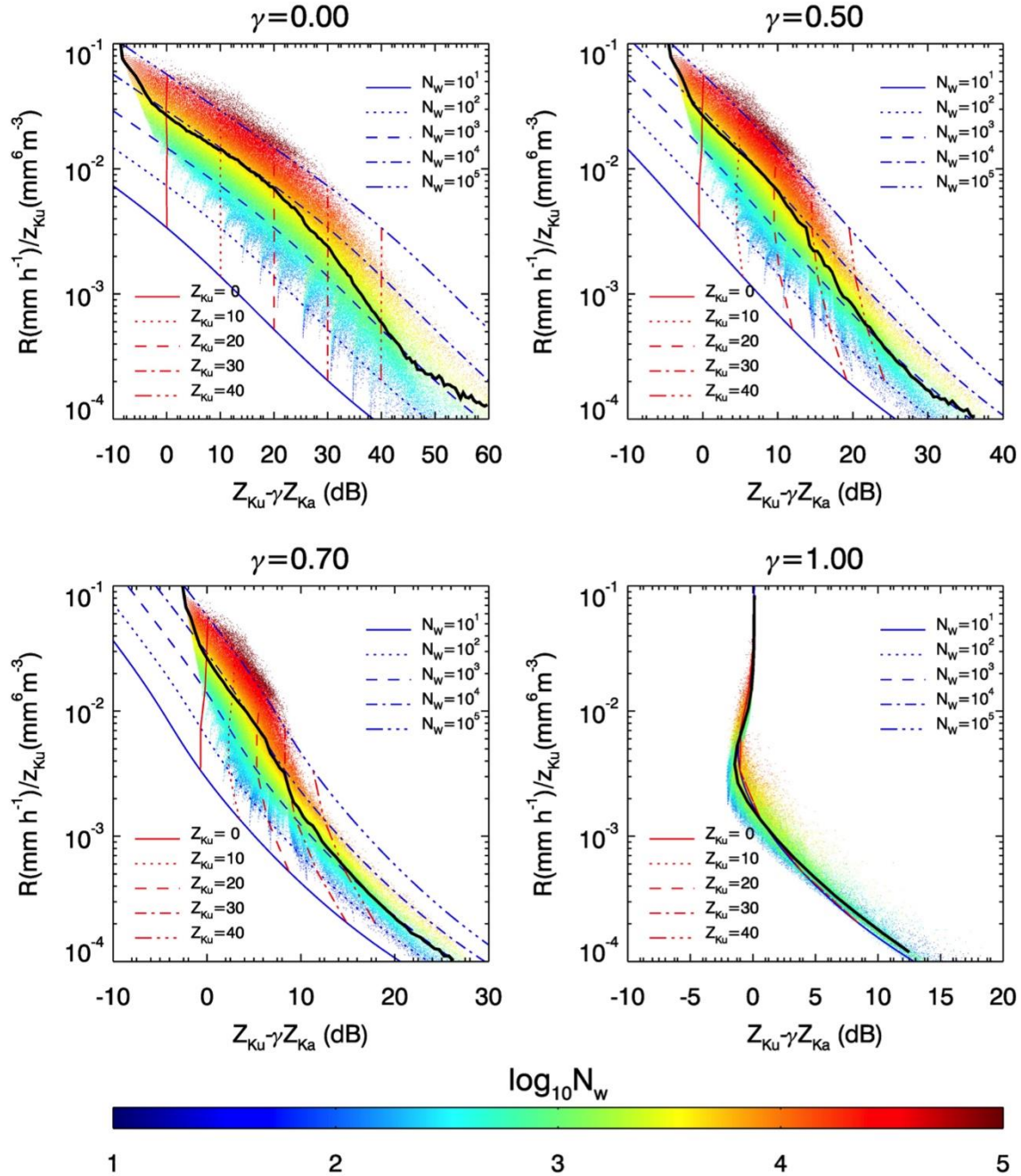


Fig.4 Scatterplots of  $Z_{\text{Ku}}$ -normalized rain rate versus modified DFR as derived from the DSD data for the cases of the weighting factor  $\gamma$  of the modified DFR equal to 0, 0.5, 0.7 and 1. Colors of the data points depict  $N_w$  values derived from the same DSD data. The mean values of the data are given by the thick dark curves. Theoretical model computations, represented by blue and red curves, are provided as the DSD is modeled as the gamma distributions with a fixed  $\mu$  of 3 and  $N_w$  ranging from 10 to  $10^5$  in  $\text{mm}^{-1}\text{m}^{-3}$ . Contours of  $Z_{\text{Ku}}$  at the values from 0 to 40 dB (red curves) are plotted as well for reference.



1

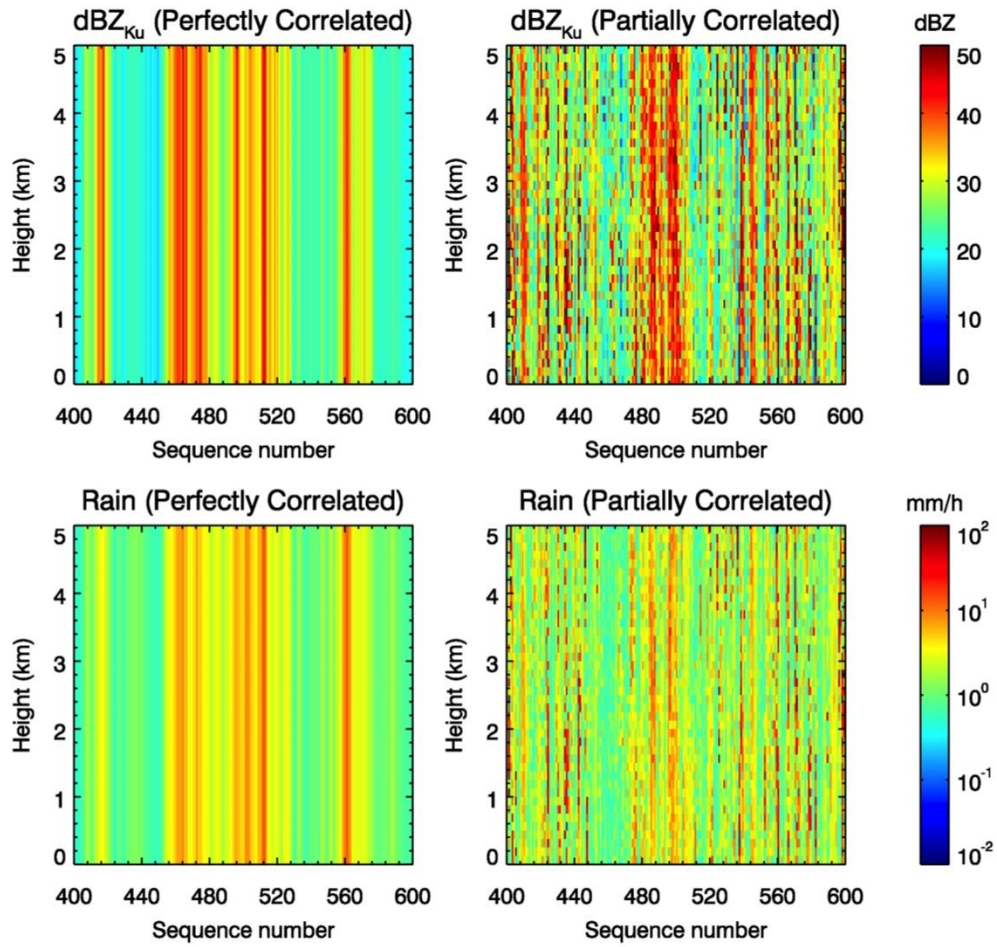


Fig.5 Ku-band radar reflectivities (top panels) and rain rate (bottom panels) simulated from a segment of the DSD profiles generated from measured DSD data. Homogeneously vertical DSD profiles are given in the left column while the non-uniform DSD profiles are provided in the right column.

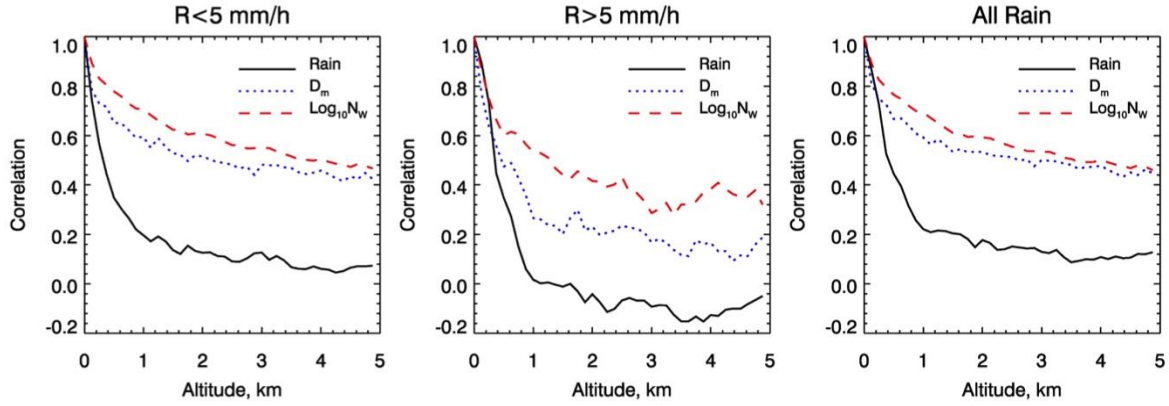


Fig.6 Averaged spatial correlations of rain rate,  $D_m$  and  $\log_{10}N_w$  for the non-uniform DSD profiles between radar range heights and surface. Results from three rain ranges, i.e.,  $R < 5$ ,  $R \geq 5$  and  $R > 0$  mm/h (all rain), are provided for approximately representing stratiform, convective and their combined systems.



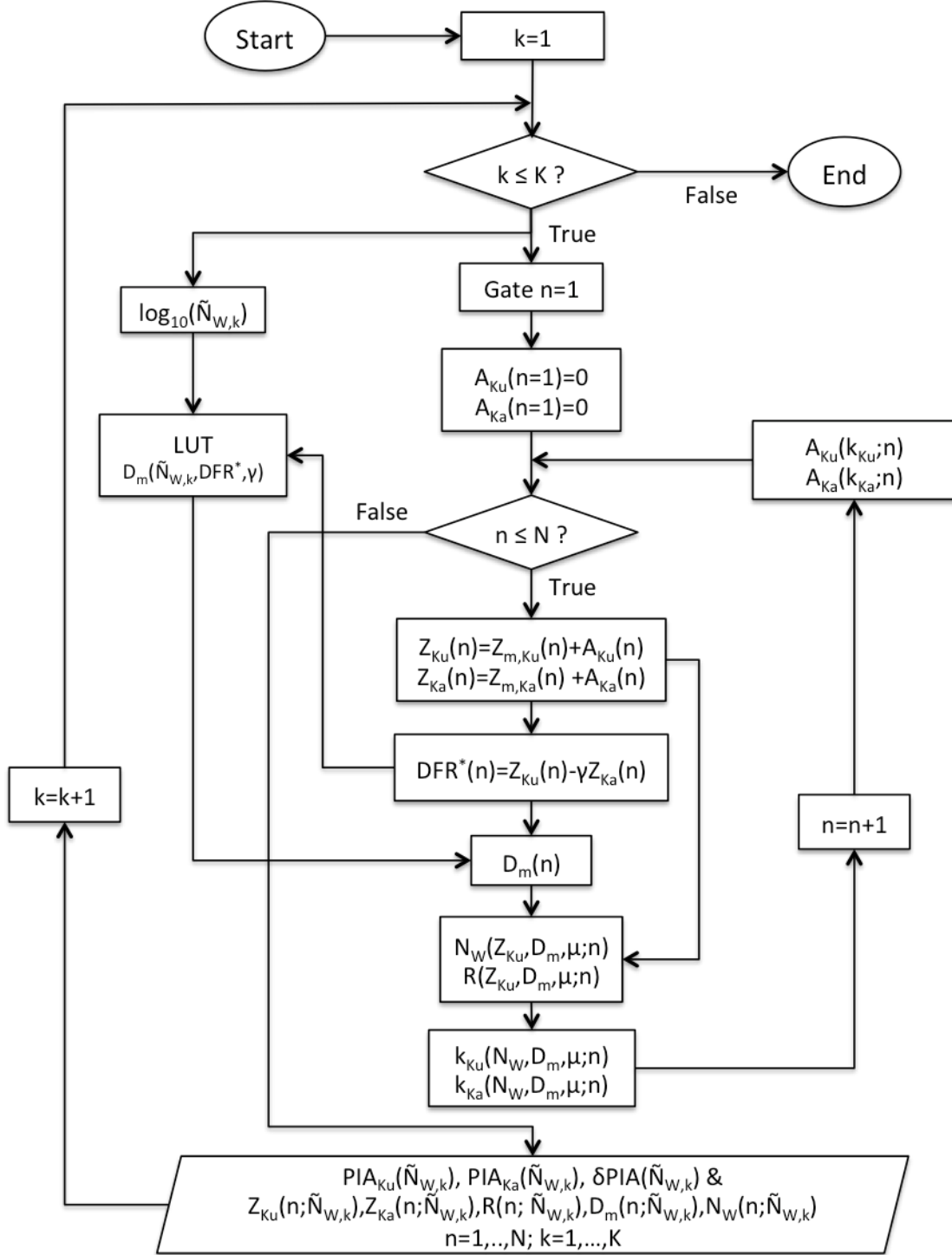


Fig.7 Flowchart of the modified dual-wavelength technique (DFR\*) for retrieval of DSD parameters and rain rate. Outer-loop variable  $k$  goes from 1 to  $K$  to provide equal-spaced values of  $\log_{10}(\tilde{N}_{w,k})$  at each step while inner-loop variable  $n$ , running from 1 to  $N$ , represents radar range gates at which the retrievals are carried out.

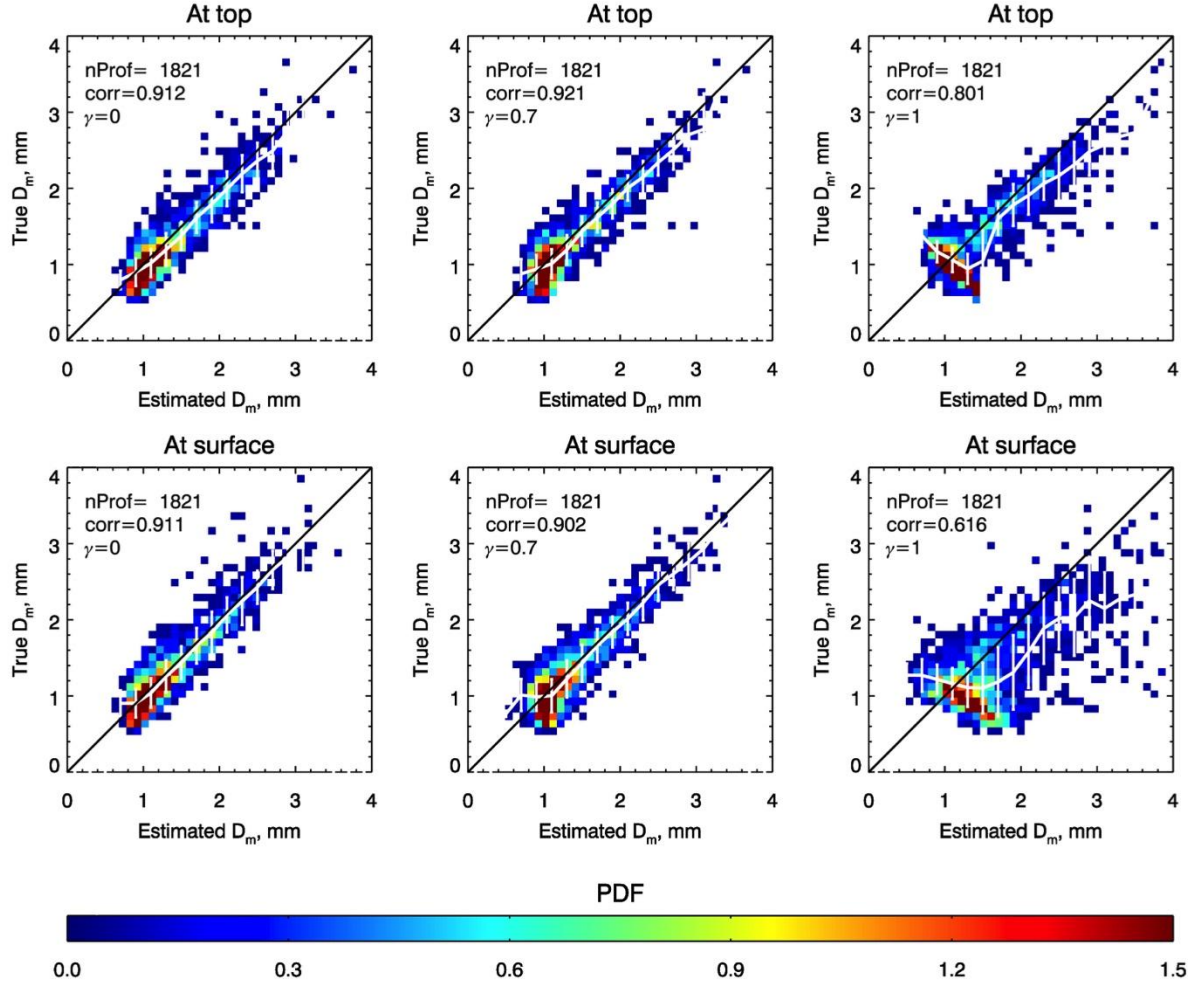


Fig.8 Two-dimensional probability density functions of  $D_m$  estimated by the modified DFR with  $\gamma$  of 0 and 0.7 (left and middle columns) as well as the standard DFR ( $\gamma=1$ ) (right column) with the true  $D_m$  for the range gate at the rain top (top row) and at the surface (bottom row). The one-to-one lines are given by the black solid curves while the means and twice the standard deviations of the data are given by the white solid curves and vertical bars, respectively. For both the modified and standard DFR methods, the forward recursive approach is used and applied to the non-uniform DSD profiles. An unbiased statistical  $\delta$ PIA model with the standard deviation of 0.8 dB is assumed.

1

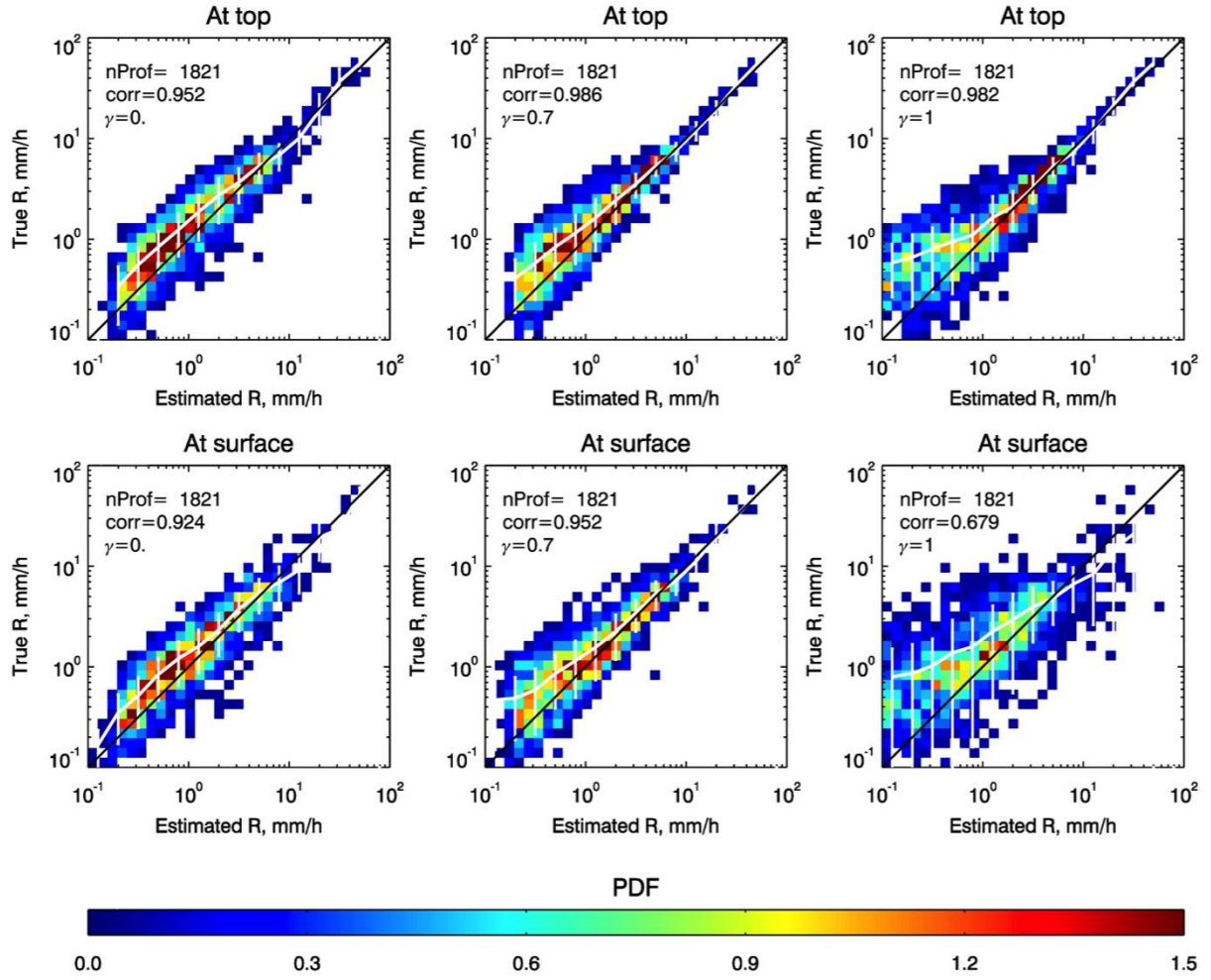


Fig.9 Two-dimensional probability density functions of rain rate estimated by the modified DFR with  $\gamma$  of 0 and 0.7 (left and middle columns) as well as the standard DFR ( $\gamma=1$ ) (right column) with the true rain rate for a range gate at the rain top (top row) and at the surface (bottom row). The one-to-one lines are given by the black solid curves while the means and twice the standard deviations of the data are given by the white solid curves and vertical bars, respectively. The non-uniform DSD profiles are assumed and the forward recursive approach is applied for both the standard and modified DFR methods. An unbiased statistical  $\delta$ PIA model with the standard deviation of 0.8 dB is assumed.

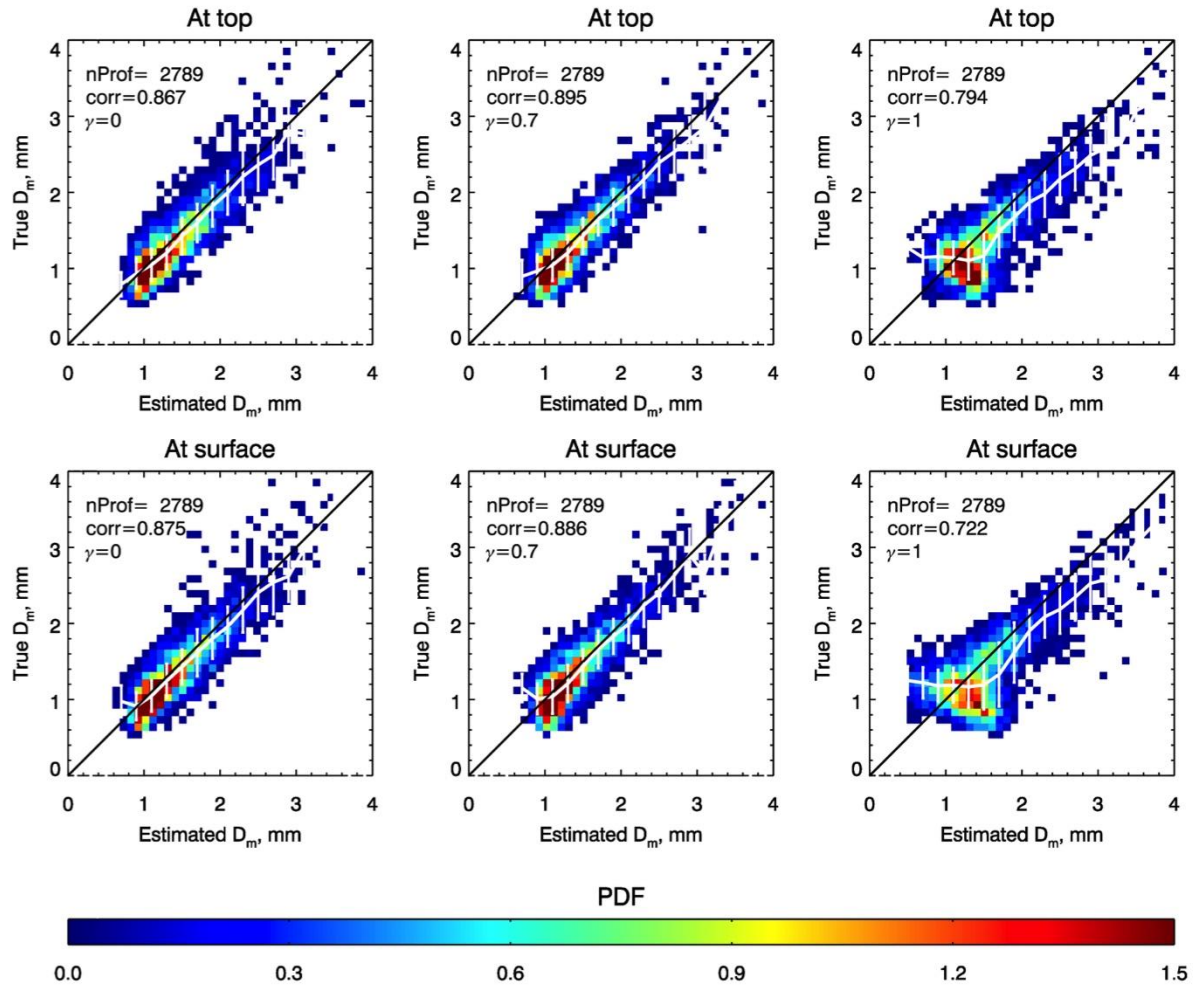


Fig.10 Two-dimensional probability density functions of  $D_m$  estimated by the modified DFR with  $\gamma$  of 0 and 0.7 (left and middle columns) as well as the standard DFR ( $\gamma=1$ ) (right column) with the true  $D_m$  for a range gate at the rain top (top row) and at the surface (bottom row). The one-to-one lines are given by the black solid curves while the means and twice the standard deviations of the data are given by the white solid curves and vertical bars, respectively. The backward recursive approach is applied in all cases to the non-uniform DSD profiles. Unbiased statistical PIA and  $\delta$ PIA models with the standard deviations of 2 dB and 0.8 dB are assumed, respectively.

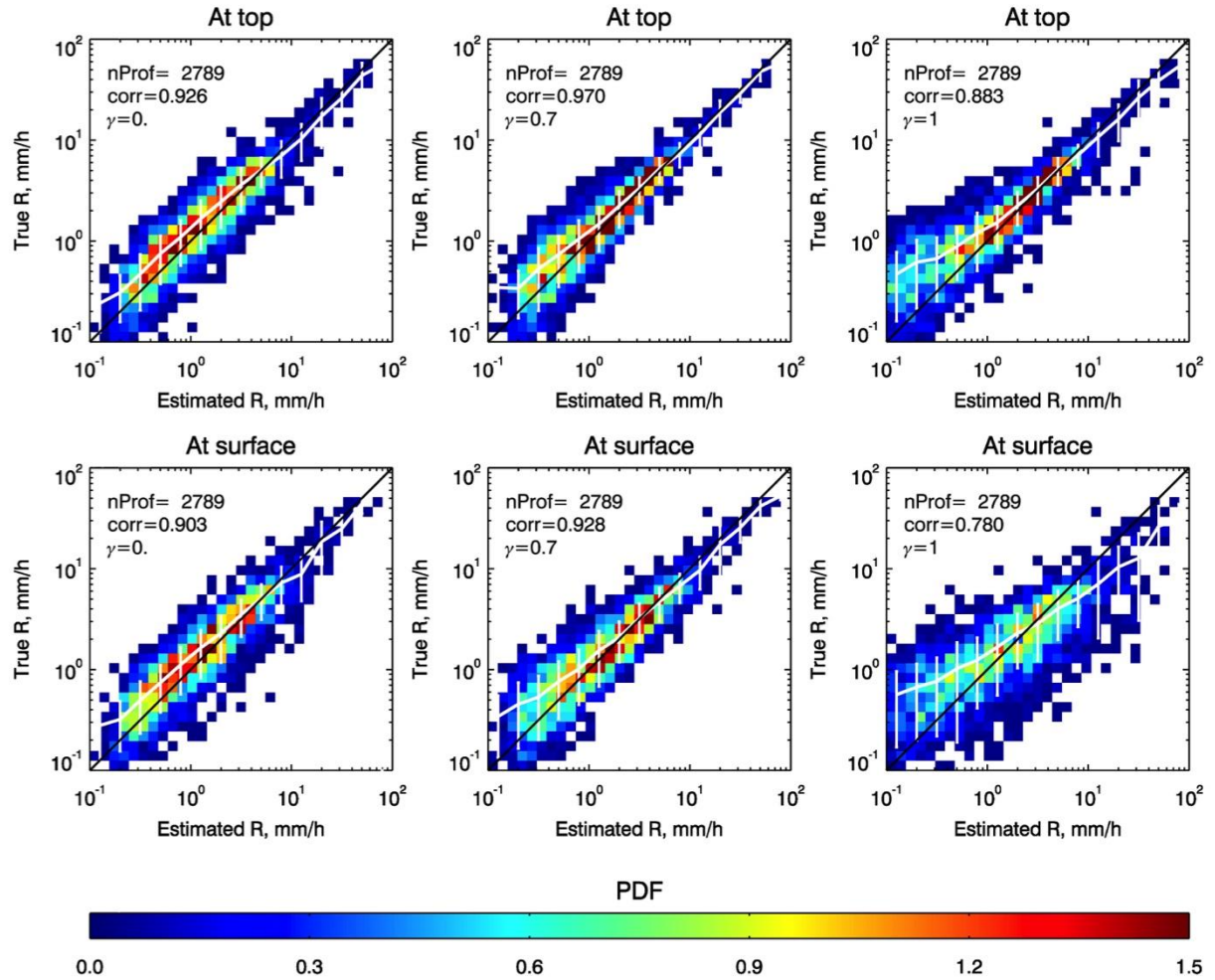


Fig.11 Two-dimensional probability density functions of rain rate estimated by the modified DFR with  $\gamma$  of 0 and 0.7 (left and middle columns) as well as the standard DFR ( $\gamma=1$ ) (right column) with the true rain rate for a range gate at the rain top (top row) and at the surface (bottom row). The one-to-one lines are given by the black solid curves while the means and twice the standard deviations of the data are given by the white solid curves and vertical bars, respectively. The backward recursive approach is applied to the non-uniform DSD profiles. Unbiased statistical PIA and  $\delta$ PIA statistical models with the standard deviations of 2 dB and 0.8 dB are assumed, respectively.